



Chinese Pharmaceutical Association
Institute of Materia Medica, Chinese Academy of Medical Sciences

Acta Pharmaceutica Sinica B

www.elsevier.com/locate/apsb
www.sciencedirect.com



ORIGINAL ARTICLE

A tactical nanomissile mobilizing antitumor immunity enables neoadjuvant chemotherapy to minimize postsurgical tumor metastasis and recurrence



Tao He, Mingxing Hu, Shun Yao Zhu, Meiling Shen, Xiaorong Kou, Xiuqi Liang, Lu Li, Xinchao Li, Miaomiao Zhang, Qinjie Wu*, Changyang Gong*

State Key Laboratory of Biotherapy and Cancer Center, West China Hospital, Sichuan University, Chengdu 610041, China

Received 6 April 2022; received in revised form 7 June 2022; accepted 19 June 2022

KEY WORDS

Neoadjuvant;
Chemotherapy;
Immunotherapy;
Mitoxantrone;
Vaccine;
Azobenzene derivatives;
Reduction responsive;
Melanoma

Abstract Neoadjuvant chemotherapy has become an indispensable weapon against high-risk resectable cancers, which benefits from tumor downstaging. However, the utility of chemotherapeutics alone as a neoadjuvant agent is incapable of generating durable therapeutic benefits to prevent postsurgical tumor metastasis and recurrence. Herein, a tactical nanomissile (TALE), equipped with a guidance system (PD-L1 monoclonal antibody), ammunition (mitoxantrone, Mit), and projectile bodies (tertiary amines modified azobenzene derivatives), is designed as a neoadjuvant chemo-immunotherapy setting, which aims at targeting tumor cells, and fast-releasing Mit owing to the intracellular azoreductase, thereby inducing immunogenic tumor cells death, and forming an *in situ* tumor vaccine containing damage-associated molecular patterns and multiple tumor antigen epitopes to mobilize the immune system. The formed *in situ* tumor vaccine can recruit and activate antigen-presenting cells, and ultimately increase the infiltration of CD8⁺ T cells while reversing the immunosuppression microenvironment. Moreover, this approach provokes a robust systemic immune response and immunological memory, as evidenced by preventing 83.3% of mice from postsurgical metastasis or recurrence in the B16–F10 tumor mouse model. Collectively, our results highlight the potential of TALE as a neoadjuvant chemo-immunotherapy paradigm that can not only debulk tumors but generate a long-term immunosurveillance to maximize the durable benefits of neoadjuvant chemotherapy.

*Corresponding authors. Tel./fax: +86 13541158521 (Changyang Gong), +86 13402823774 (Qinjie Wu).

E-mail addresses: cellwj@163.com (Qinjie Wu), chyong14@163.com (Changyang Gong).

Peer review under responsibility of Chinese Pharmaceutical Association and Institute of Materia Medica, Chinese Academy of Medical Sciences.

<https://doi.org/10.1016/j.apsb.2022.09.017>

2211-3835 © 2023 Chinese Pharmaceutical Association and Institute of Materia Medica, Chinese Academy of Medical Sciences. Production and hosting by Elsevier B.V. This is an open access article under the CC BY-NC-ND license (<http://creativecommons.org/licenses/by-nc-nd/4.0/>).

1. Introduction

Surgery remains the preferred treatment option for most patients with solid tumors. However, many high-risk resectable cancers are associated with high rates of recurrence after surgery, such as melanoma¹, hepatocellular carcinoma², and urothelial carcinoma³. Neoadjuvant chemotherapy refers to the combined chemotherapy for several courses before radical surgery of malignant tumors to reduce tumor volumes so as to remove tumor cells more thoroughly^{4,5}. Due to the potential of tumor downstaging and eliminating a small number of tumor cells in the blood or lymph circulation preoperatively, neoadjuvant chemotherapy has created an unparalleled opportunity for patients with high-risk resectable cancers^{6,7}. However, the advantages of chemotherapeutics as neoadjuvant with respect to reducing tumor stages are frequently offset by considerable toxicity and difficulty in generating long-term systemic immunosurveillance that can be transformed into durable therapeutic benefits⁸. Of note, micrometastasis and residual tumor micro-infiltration as sources of postsurgical metastasis and relapse are often the causes of the high mortality^{9–11}. Thereby, it is imperative to explore a neoadjuvant therapy strategy that can not only debulk tumors preoperatively, but also continuously inhibit tumor metastasis and recurrence to enlarge the advantages of neoadjuvant chemotherapy.

Cancer immunotherapies, including cancer vaccines, immune checkpoint inhibitors, and adoptive cell therapy, have been extensively developed in the modern oncology era. In particular, cancer vaccines composed of tumor-associated antigens (TAAs) or neoantigens and immune adjuvants are designed to mobilize the immune system against tumors, and hold promise for the durable treatment of cancer^{12–14}. However, TAAs may also be expressed in healthy tissues and exhibit low affinity to T cells¹³. On the other hand, although neoantigens overcome the above shortcomings of TAAs, the cumbersome, expensive identification process and low immunogenicity of neoantigens limit their further application¹⁵. Moreover, the slow acquisition and working process of cancer vaccines are contrary to rapid cancer progression, which may further lead to the denial of surgical opportunities. Compared with the complex *in vitro* tumor antigen preparation and limited antigen epitopes, the formation of a cancer vaccine *in situ* to enhance antitumor immunity may be an attractive alternative, since *in situ* tumors contain multiple tumor-specific antigen epitopes, which enable the generation of broad and durable immune responses. In light of the above findings, strategies aim at both *in situ* tumor killing and vaccine formation could be expected to achieve both reduced tumor burden and enhanced systemic antitumor immune response preoperatively.

One approach to this aim may involve the local promotion of immunogenic tumor phenotypes. For example, some chemotherapeutic drugs ultimately stimulated T cell immune surveillance of tumors by empowering immunogenic cell death (ICD), which enhanced the uptake and cross-presentation of tumor antigens by antigen-presenting cells as a result of releasing damage-associated

molecular patterns (DAMPs), including calreticulin (CRT), ATP and high mobility group Box 1 protein (HMGB1)^{16–20}. In addition, prior chemotherapy with anthracycline antibiotics increased the ratio of cytotoxic T cells to regulatory T cells (Tregs) in the tumor microenvironment, which is related to the improved clinical outcome²¹. Nevertheless, chemotherapeutics can only marginally extend survival and are often accompanied by high doses and severe side effects²². Despite the low remission rate, these chemotherapeutics deserve reconsideration, especially when combined with immunotherapy. For example, combining checkpoint blockade with immunogenic chemotherapeutics has greatly expanded in improving the low objective remission rate of checkpoint inhibitors²³. The synergistic combination of chemotherapy and immunotherapy is considered more effective than the two methods alone^{2,24}. In addition, engineered nanomedicine delivery systems are gradually recognized as towardly approaches for the delivery of chemotherapeutics and biologics, with optimized pharmaceutical properties and reduced off-target adverse effects^{25–27}. In particular, stimuli-responsive nanomedicines that can accurately release drugs under specific conditions are more likely to succeed in clinical treatment due to the temporal and spatial specificity of drug release^{28,29}.

Herein, a tactical nanomissile (TALE) was designed as a neoadjuvant chemo-immunotherapy approach that elicited *in situ* tumor vaccines to stimulate antitumor immune response and immunological memory, thereby minimizing postoperative tumor metastasis and recurrence. This orchestrated TALE comprises three functional ingredients, including a guidance system (anti-programmed death-ligand 1, aPD-L1), ammunition (mitoxantrone, Mit), and projectile bodies with both adjuvant effect and tumor intracellular azoreductase-responsiveness (tertiary amines modified azobenzene derivatives, AZO), hereafter referred to as MPAL (mitoxantrone@anti-PD-L1/azobenzene-lipo). After systemic administration, MPAL targets tumor cells through surface-embedded aPD-L1 and meanwhile switches off the immunosuppression caused by the PD-1/PD-L1 pathway. Subsequently, MPAL could disintegrate in tumor cells rich in azoreductase due to the cleavage of azo bonds, achieving the intracellular burst release of Mit. Then, ICD induced by Mit is amplified by tertiary amine compounds which can cause the rupture of the endomembrane or the activation of interferon genes in APCs as immune adjuvants³⁰, thereby generating an *in situ* tumor vaccine to stimulate the host immune system. Thus, our TALE achieved both tumor regression and enhanced antitumor immunity that can be transformed into long-term therapeutic benefits without further adjuvant therapy, which was inescapably required after surgery in current neoadjuvant chemotherapy. The tactic presented here provides a promising approach for patients with high-risk resectable cancers, that can minimize preoperative treatment interval and hold prospects in clinical neoadjuvant chemo-immunotherapy for improving the prognosis of patients through the bolstered systemic antitumor immunity and immunological memory.

2. Materials and methods

2.1. Materials and reagents

Mitoxantrone hydrochloride was purchased from Dalian Meilun Biotechnology Co., Ltd. (Dalian, China) Recombinant mouse GM-CSF and IL-4 were obtained from Peprotech (Rocky Hill, NJ, USA). ATP assay system bioluminescence detection kit was purchased from Promega Corporation (Madison, WI, USA). Mouse HMGB1 ELISA kit was purchased from Enzyme-linked Biotechnology Co., Ltd. (Shanghai, China). Anti-calreticulin antibody and goat anti-rabbit IgG H&L (FITC) were obtained from Abcam (Cambridge, UK). 4-Dodecyl aniline (99.9%), phenol (99.9%), 1, 3-dibromopropane (99.9%), diethylamine (99.9%), hydrochloric acid (HCl, 37%), etc. were purchased from Chron Chemicals Co., Ltd. (Chengdu, China). Sodium nitrite (NaNO_2 , >98%), potassium iodide (KI, > 98%), potassium carbonate (K_2CO_3 , >98%), dithionite ($\text{Na}_2\text{S}_2\text{O}_4$, >98%), and β -mercaptoethanol, etc. were purchased from Macklin Co., Ltd. (Shanghai, China). Cholesterol (CHOL), DSPE-mPEG2000, and DSPE-PEG2000-NHS were obtained from Advanced Vehicle Technology Co., Ltd. (Shanghai, China). DiD was obtained from Bosunlife Biotechnology Co., Ltd. (Beijing, China). Antibodies used in flow cytometry analysis were purchased from Biolegend (San Diego, CA, USA), Abcam (Cambridge, UK), Bioss Co., Ltd. (Beijing, China), or eBioscience (San Diego, CA, USA). Detailed sources of all antibodies are provided in Supporting Information Table S1.

2.2. Cells and animals

B16–F10 cells were purchased from American Type Culture Collection (USA). B16–F10 cells expressing luciferase (B16–F10-Luc) were obtained from iCell Bioscience Co., Ltd. (Shanghai, China). B16–F10 and B16–F10-Luc cells were both cultured in Roswell Park Memorial Institute (RPMI) medium (Gibco Invitrogen, USA) supplemented with 10% (*v/v*) fetal bovine serum (FBS) and streptomycin-penicillin (1%, *v/v*) at 37 °C under a humidified atmosphere containing 5% CO_2 .

Female C57BL/6 mice (6–8 weeks, 18–22 g) were provided by the Laboratory Animal Center of Sichuan University (Chengdu, China) and kept in specific pathogen-free conditions. All animal experiments were conducted according to the protocols approved by the provisions of Institutional Animal Care and Treatment Committee of Sichuan University.

2.3. Confirmation of Mit-induced ICD

B16–F10 cells were seeded in 12-well plates at a density of 1×10^5 cells per well. Then, the supernatant was replaced with medium containing the indicated concentrations of Mit. 24 h later, cells were incubated with rabbit anti-mouse CRT antibody (Abcam, Cambridge, UK). After washed three times, cells were stained with Alexa Fluoro 488 conjugated goat anti-rabbit IgG H&L (Abcam, Cambridge, UK) and DAPI, followed by detection using flow cytometry and confocal microscope. In addition, HMGB1 and ATP in the supernatant were measured by HMGB1 ELISA kit (Enzyme-linked Biotechnology) and ATP assay system bioluminescence detection kit (Promega), respectively.

To test whether the B16–F10 cells treated by Mit induced DC maturation, bone marrow-derived dendritic cells (BMDCs) were obtained according to the previous method^{31,32}. The cultured BMDCs were plated in a 12-well plate at 1×10^6 cells per well, and co-cultured with B16–F10 cells that were pretreated with Mit (1 $\mu\text{mol/L}$) for 24 h. BMDCs co-cultured with live B16–F10 was used as a control. Then, the cells were stained with PE anti-mouse CD11c antibody (Biolegend) and APC anti-mouse CD86 antibody (Biolegend), followed by analysis using flow cytometry (Agilent, NovoCyte, USA).

B16–F10 cells pretreated with Mit (1 $\mu\text{mol/L}$) or phosphate buffered saline (PBS) were subcutaneously immunized to female C57BL/6 mice on days 0 and 14. On Day 21, untreated B16–F10 cells were inoculated into the opposite side of the back of immunized mice at a dose of 1×10^6 cells per mouse, and the tumor volume was recorded every 2 days. All animal experiments complied with the Guide of the Institutional Animal Care and Treatment Committee of Sichuan University (Chengdu, China).

2.4. Synthesis of AZO

4-Dodecylaniline (2.013 g, 7.7 mmol) was dissolved in dilute hydrochloric acid (100 mL) and transferred to an ice-salt bath for pre-cooling. Then, sodium nitrite (0.504 g, 7.3 mmol) was dissolved in distilled deionized water (20 mL) and added dropwise to the 4-dodecylaniline solution to react for 1 h. Subsequently, phenol (0.725 g, 7.7 mmol) was dissolved in distilled deionized water (20 mL) and added dropwise to the system. Sodium carbonate was then used to adjust the pH of the reaction system to 8, and the yellow azobenzene derivative was immediately precipitated. The residue was washed twice with water, dried over anhydrous magnesium sulfate, and eluted by column chromatography to give 4-((4-dodecylphenyl) diaziny) phenol (2.200 g). Yield: 78.6%. $^1\text{H NMR}$: (400 MHz, DMSO-d_6) δ 10.26 (s, 1H), 7.81–7.71 (m, 4H), 7.42–7.31 (m, 2H), 6.97–6.89 (m, 2H), 2.71–2.56 (m, 2H), 1.68–1.52 (m, 2H), 1.23 (s, 18H), 0.89–0.82 (m, 3H).

4-((4-Dodecylphenyl) diaziny) phenol (2.200 g 6.0 mmol), KI (0.099 g, 0.60 mmol), K_2CO_3 (0.831 g, 6.01 mmol) and 1,3-dibromopropane (2 mL) were heated and refluxed overnight at 50 °C. The mixture was washed with saturated brine, and concentrated by rotary evaporation. The product was purified by column chromatography and vacuum drying to obtain 2.3 g of the (*E*)-1-(4-(3-bromopropoxy) phenyl)-2-(4-dodecylphenyl) diene, with a yield of 78.0%. $^1\text{H NMR}$ (400 MHz, chloroform-*d*) δ 7.90 (d, *J* = 8.4 Hz, 2H), 7.80 (d, *J* = 8.4 Hz, 2H), 7.30 (d, *J* = 8.4 Hz, 2H), 7.01 (d, *J* = 8.4 Hz, 2H), 4.20 (d, *J* = 6.4 Hz, 2H), 3.63 (t, *J* = 6.4 Hz, 2H), 2.72–2.63 (m, 2H), 2.42–2.32 (m, 2H), 1.65 (p, *J* = 7.4 Hz, 2H), 1.26 (s, 18H), 0.90–0.85 (m, 3H).

The product obtained above in absolute ethanol (30 mL) was added into excess diethylamine. After refluxed overnight at 60 °C, the mixture was purified by column chromatography and vacuum drying, obtaining a yellow oily azo derivative (AZO, 1.3 g). Yield: 57.5%. $^1\text{H NMR}$ (400 MHz, chloroform-*d*) δ 7.91–7.86 (m, 2H), 7.81–7.76 (m, 2H), 7.32–7.27 (m, 2H), 7.05–6.94 (m, 2H), 4.11 (d, *J* = 6.4 Hz, 2H), 2.75–2.54 (m, 8H), 2.02 (p, *J* = 6.4 Hz, 2H), 1.74–1.57 (m, 2H), 1.38–1.19 (m, 18H), 1.09 (d, *J* = 7.2 Hz, 6H), 0.93–0.81 (m, 3H). $^{13}\text{C NMR}$ (101 MHz, chloroform-*d*) δ 161.25, 151.04, 147.06, 145.83, 129.03, 124.54, 122.51, 114.68, 77.21, 49.36, 47.05, 35.87, 31.92, 31.33, 29.67, 29.65, 29.64, 29.59,

29.50, 29.35, 29.28, 22.69, 14.12, 11.44. HRMS (ESI⁺, *m/z*): [C31H50N3O]⁺ (M + H)⁺ Calcd. 480.3948, Found 480.3968.

2.5. MPAL preparation and characterization

AZO, cholesterol and DSPE-mPEG2000 were dissolved in a mixed solvent of chloroform and methanol according to the molar ratio of AZO:cholesterol:DSPE-mPEG2000 = 50:45:5, 60:35:5, 70:25:5, 80:15:5 and 90:5:5. The solvent was evaporated to form a uniform film at 40 °C which was further dried overnight in a vacuum desiccator. Afterwards, the obtained film was hydrated with 2 mL of 150 mmol/L ammonium sulfate solution in a 65 °C water bath for 30 min. Then, the mixture was sonicated at 104 W followed by strained 15 times through a 100 nm polycarbonate membrane to obtain AZO-Lipo. Before encapsulating mitoxantrone, the ammonium sulfate outside the liposome was replaced with PBS by dialysis (MW = 3500). Mit@AZO-Lipo (MAL) with different AZO molar ratios were obtained by incubating AZO-Lipo with Mit at 65 °C for 1 h in the drug-to-lipid ratio of 1:10, and purified using a G-25 Sephadex column. To determine the Mit encapsulation efficiency (EE) and drug loading (DL) of MAL with different AZO molar ratios, freeze-drying, and ultraviolet–visible spectrophotometry were used, and the calculation Eqs. (1) and (2) of which are as follows:

$$EE (\%) = \frac{W_{\text{Mit in MAL}}}{W_{\text{Total Mit}}} \times 100 \quad (1)$$

$$DL (\%) = \frac{W_{\text{Mit in MAL}}}{W_{\text{MAL}}} \times 100 \quad (2)$$

where $W_{\text{Mit in MAL}}$ is the weight of encapsulated Mit in MAL; $W_{\text{total Mit}}$ is the weight of Mit added; W_{MAL} is the weight of MAL.

Mit@aPD-L1/AZO-Lipo (MPAL) was prepared by a described coupling method³³. In brief, DSPE-PEG2000-NHS and mPEG2000-DSPE were mixed at a 1:4 molar ratio to prepare a film, followed by hydrating with PBS containing aPD-L1 (Biolegend). The coupling reaction was carried out by ester conjugation between aPD-L1 and the terminal active ester of DSPE-PEG2000-NHS. To obtain the MPAL, DSPE-PEG2000-aPD-L1 was transferred into preformed MAL for stirring at room temperature overnight, and then purified by ultrafiltration (300 K, Millipore). The concentration of aPD-L1 in MPAL was detected by BCA reagent assay according to the instructions. The hydrated particle size of MPAL was measured using NanoZS ZEN 3600 (Malvern, UK), and the morphology of which was observed by transmission electron microscopy (TEM, JEM-100CX, Japan) and high-resolution field emission scanning electron microscopy (FESEM, Aztec Live ULTIM, USA). The preparation process of Mit@Lipo (ML) and Mit@aPD-L1-Lipo (MPL) referred to MAL and MPAL, but the difference was that DSPC replaced AZO.

To test the insertion efficiency of aPD-L1, 1 μL of PE-labeled goat anti-rat IgG H&L (Abcam) was added to 100 μL of MPAL and incubated for 30 min at room temperature. After that, MPAL was washed twice with PBS by ultrafiltration (300 K, Sartorius). The insertion efficiency of aPD-L1 in MPAL was detected by flow cytometry (Agilent).

2.6. Azoreductase-sensitive evaluation of MPAL

Na₂S₂O₄ was used as a reductase mimic reagent^{34,35} in tumors to evaluate the azoreductase sensitivity of MPAL. AL or MPAL was treated with Na₂S₂O₄, and then the reduced sensitivity of MPAL

was analyzed by the following methods: (1) Color changes of AL were observed before and after treatment with Na₂S₂O₄; (2) UV–Visible (UV–Vis) absorption of MPAL ranged from 200 to 500 nm; (3) Changes in hydrated particle size and morphology were detected using NanoZS ZEN 3600 and TEM respectively; and (4) the azoreductase-responsive release behavior of Mit from MPAL was determined by UV–Vis spectrophotometry (UV-2600, Shimadzu, Japan).

2.7. Analysis of cellular uptake and MPAL-induced ICD

B16–F10 cells were seeded in 12-well plates. 12 h later, the supernatant was replaced with Mit, MAL, or MPAL-containing medium at a final Mit concentration of 1 μmol/L for 0.5 h. To study competitive binding, aPD-L1 was introduced into the medium 1 h before MPAL was added. After incubation, cells were washed twice with PBS, and the proportion of Mit positive cells was analyzed using flow cytometry (Agilent).

B16–F10 cells were seeded in 12-well plates at a density of 1×10^5 cells per well. Then, the supernatant was replaced with medium containing the indicated concentrations of MPAL. 24 h later, CRT exposure and ATP release were detected using the same methods as described above. For HMGB1 detection, cells were permeabilized, fixed, and then stained with FITC conjugated anti-mouse HMGB1 antibody (Bioss) before flow cytometric detection.

2.8. Biodistribution of liposomes

DiD@AZO-Lipo (DiD-AL) and DiD@aPD-L1/AZO-Lipo (DiD-PAL) were prepared with DiD introduced to the solution containing AZO, DSPE-PEG2K, and cholesterol at a molar ratio of AZO:DiD = 120:1. The subsequent preparation process refers to the preparation method of AL or MPAL. B16–F10 tumor-bearing C57BL/6 mice (tumor volume = 500 mm³) were intravenously injected with free DiD, DiD-AL, and DiD-PAL at 150 μg/kg of DiD. After 24 h of administration, the separated heart, liver, spleen, lung, kidney, and tumor were subjected to *ex vivo* fluorescence imaging (PerkinElmer, IVIS Lumina Series III, USA), and the DiD fluorescence intensity in each tissue was recorded.

2.9. In vivo tumor model

In the B16–F10 subcutaneous tumor model, female C57BL/6 mice were divided into 7 groups ($n = 5$) when the tumor volume reached 50–100 mm³ (on Day 6 after tumor inoculation) and treated with PBS, Mit, Mit&aPD-L1, ML, MPL, MAL and MPAL on Days 6, 8 and 10, respectively (Mit dose: 0.8 mg/kg, aPD-L1 dose: 1 mg/kg). The tumor size was monitored by a vernier caliper every two days, and the volume was calculated using Eq. (3):

$$\text{Volume} = 0.5 \times \text{Width}^2 \times \text{Length} \quad (3)$$

On Day 17 after inoculation, the mouse blood was collected for serum chemistry profile and major organs (heart, liver, spleen, lung, and kidney) were dissected and sectioned for histopathologic examination. The tumors were weighed and then divided into two parts: one part was fixed in 4% paraformaldehyde for subsequent paraffin sections and hematoxylin-eosin (H&E) staining. The

other part was wrapped with OCT for frozen sectioning and further TUNEL and CRT immunofluorescence staining.

To establish a lung metastatic model of melanoma, female C57BL/6 mice were intravenously injected with 5×10^5 B16–F10-Luc cells. On Day 4, mice were randomly separated into three groups ($n = 5$): PBS, MAL, and MPAL. Mice in each group were treated on Days 4, 6, and 8 after inoculation, respectively, and the treatment dose was consistent with that of the subcutaneous tumor model. On Days 11, 15, and 19, the mice were intraperitoneally injected with D-luciferin potassium salt followed by biofluorescence imaging, and recorded by the IVIS® Spectrum system (PerkinElmer). After the last imaging, the mice were euthanized and the lung in each group was collected for weighing, photographing, and counting the number of tumor nodules. Then, the lungs were immersed in 4% paraformaldehyde for further H&E staining.

To evaluate the therapeutic effects on postsurgical metastasis of melanoma, the B16–F10 subcutaneous tumor model was established. When the tumor volume reached 50–100 mm³ (Day –12), the mice were randomly divided into three groups ($n = 5$): PBS, MAL, and MPAL. Mice in each group were treated on 5 (Day –7), 7 (Day –5) and 9 (Day –3) days after inoculation, respectively. On Day 11 (Day –1), tumors in the right back of all mice were surgically resected and the injured skins were sutured with 5–0 silk sutures. One day after surgery, B16–F10 tumors were inoculated into the contralateral side of each mouse. The tumor size was measured by a vernier caliper every other day. On Day 19 after inoculation of contralateral tumors, mice in each group were sacrificed, and the tumors were removed and weighed. A similar experiment was carried out for a model of melanoma postsurgical recurrence, except that the mice after the surgery kept tumor-free for 10 days prior to being rechallenged. On Day 19 after being rechallenged, the tumors were collected and weighed.

2.10. Flow cytometry and ELISA assay analysis for *in vivo* immune responses

In the B16–F10 subcutaneous tumor model, female C57BL/6 mice were divided into 3 groups ($n = 5$) and treated with PBS, MAL, and MPAL on Days 6, 8, and 10, respectively. The day after the last treatment, serum samples were collected for the detection of TNF- α and IFN- γ by ELISA kits following vendor protocols. Tumors in each group were excised, cut into small pieces, and filtered with a 70 μ m cell sieve to prepare a single-cell suspension. After removing the erythrocyte with Ack lysis buffer, the cell samples were washed and stained with different fluorescently labeled antibodies. The following immune cells were analyzed using flow cytometer (Agilent): (i) T cells (CD3⁺CD4⁺CD8[–] or CD3⁺CD4[–]CD8⁺), (ii) Tregs (CD4⁺CD25⁺Foxp3⁺), (iii) CD91⁺ DCs (CD11⁺CD91⁺). To detect mature dendritic cells, tumor-draining lymph nodes (TDLNs) were pounded with a needle tip and followed by filtered to prepare a single-cell suspension. The obtained cells were stained and determined for CD11c⁺CD103⁺ DCs.

In the B16–F10 postsurgical metastasis model, the spleens of mice were separated, cut into pieces, and filtered *via* a 70 μ m cell sieve to prepare a single cell suspension on day 19 after the contralateral tumor was inoculated. Then, the cells were resuspended in Ack lysis buffer to remove red blood cells. After washing, the samples were stained and determined for

CD3⁺CD4⁺CD8[–] and CD3⁺CD4[–]CD8⁺ T cells. In the B16–F10 postsurgical recurrence model, the splenocyte of each mouse was obtained in the same way. After washing, single-cell was incubated with several fluorescently labeled antibodies to detect effector memory T cells (T_{EM}: CD3⁺CD8⁺CD44⁺CD62L[–]) and central memory T cells (T_{CM}: CD3⁺CD8⁺CD44⁺CD62L⁺).

2.11. Statistical analysis

Results are expressed as mean \pm standard deviation (SD), except that tumor volume is expressed as mean \pm standard error of the mean (SEM). Unpaired Student's *t*-test was used to compare two groups, and one-way ANOVA analysis was used in multiple group comparisons. A Two-way ANOVA analysis with the Bonferroni test was performed in comparing all groups. Graphpad Prism 5.0 software was used to perform statistical analysis. Significant differences are shown as follows: * $P < 0.05$, *** $P < 0.001$, ** $P < 0.01$.

3. Results and discussion

3.1. Mitoxantrone is an effective inducer of immunogenic cell death in melanoma

To provide the proof-of-concept of ICD in the melanoma neo-adjuvant chemo-immunotherapy, multiparameter evaluations to verify the ability of Mit induced ICD of B16–F10 were carried out *in vitro*. As shown in Fig. 1A, the proportion of CRT exposure in B16–F10 cells treated with Mit was significantly higher than that of normal cells, and as the concentration of Mit increased, the proportion of CRT positive cells appreciably increased. We further performed immunofluorescence staining on B16–F10 cells treated with Mit (1 μ mol/L). As shown in Fig. 1B, compared with normal cells, the Mit-treated tumor cells showed significant CRT exposure (green fluorescence). For the other two prototypical ICD-related DAMPs, HMGB1 and ATP in the supernatant of Mit-treated B16–F10 cells were detected by ELISA and bioluminescence-based ATP assay, and results in Fig. 1C and D showed a similar concentration-dependent increase trend as the results of CRT exposure. Given the critical roles of ATP, CRT, and HMGB1 in antigen-presenting cell recruitment, antigen recognition, and stimulation of maturation, we next co-incubated Mit-treated B16–F10 cells with BMDCs *in vitro*. CD86 was used as a marker to evaluate BMDCs activation. As shown in Fig. 1E, Mit-treated B16–F10 cells induced $37.7 \pm 3.2\%$ of CD86 expression on BMDCs, which was 2.3-fold higher than live B16–F10 cells, proving that dying cells can promote the maturation of professional antigen-presenting cells, and showed the potential to initiate adaptive immune responses. In addition, the ICD-inducing capacity of Mit in B16–F10 was further confirmed by a vaccination assay, which is the gold-standard approach to verify an ICD inducer³⁶. As displayed in Fig. 1F, mice were immunized twice with dying B16–F10 cells in one flank of mice within 14 days and inoculated with live B16–F10 cells in another flank after the last immunization. Results disclosed that tumor growth inhibition was more pronounced in the Mit group than that in the medium group, and Mit-treated B16–F10 cells showed enhanced protective immune responses *in vivo*, suggesting that Mit induced effective ICD in B16–F10 cells.

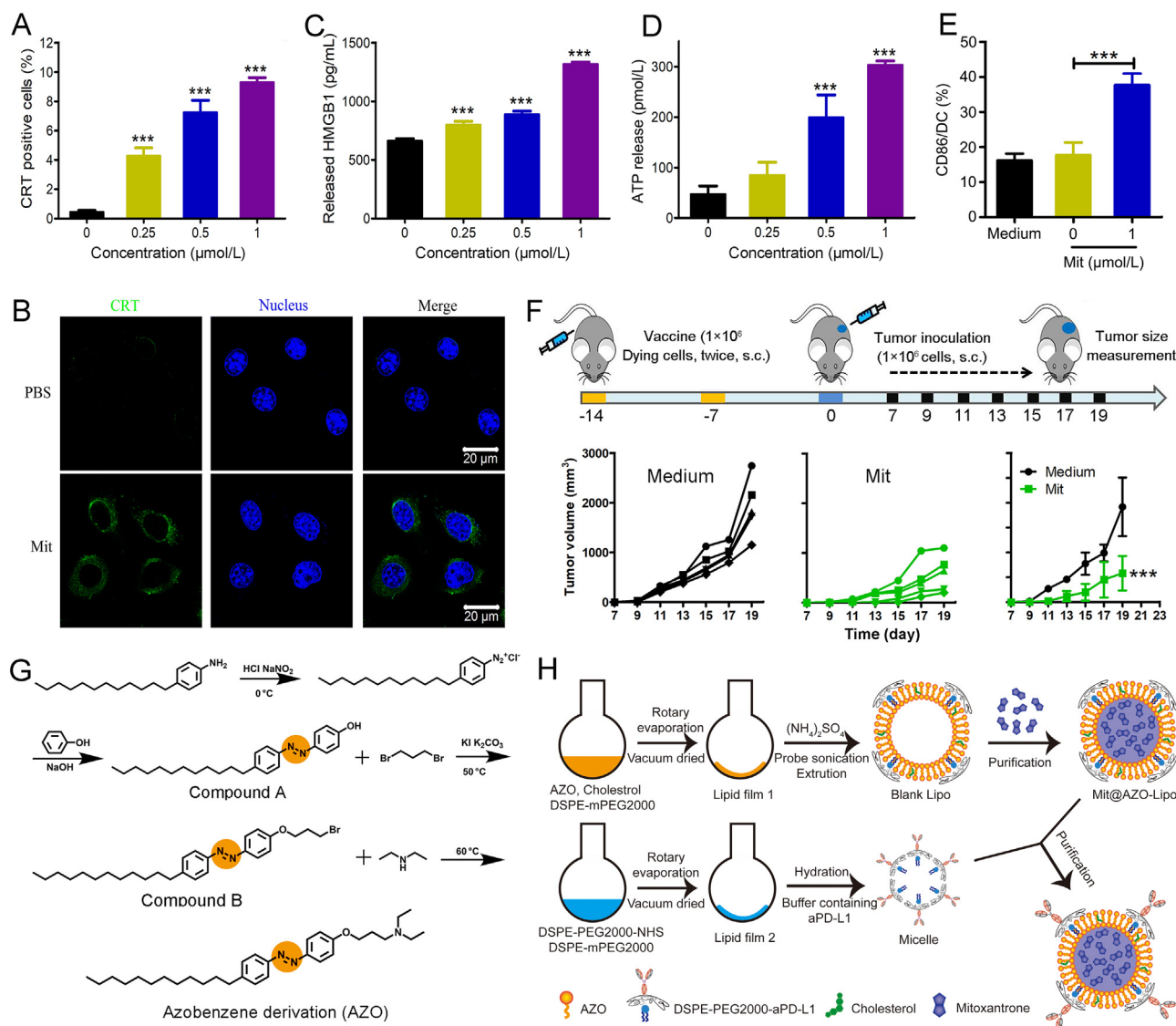


Figure 1 Mit elicited the immunogenic death of B16–F10 cells and the preparation diagram of mitoxantrone@anti-PD-L1/azobenzene-lipo (MPAL). (A) CRT detections on B16–F10 cells after being treated with different concentrations of Mit using flow cytometry. (B) CRT expression on B16–F10 cells in response to Mit was observed by confocal microscopy. Scale bar = 20 μm. Release of (C) HMGB1 and (D) ATP by B16–F10 cells after Mit treatment. (***) $P < 0.001$ indicates the statistical difference between each group and the group without Mit) (E) The expression of CD86 on BMDCs after co-cultured with Mit-treated B16–F10 cells. (F) The vaccination method was used to identify Mit-induced immunogenic B16–F10 cell death. (G) The synthesis routes of AZO. (H) Schematic illustration of the preparation steps of MPAL. Data are presented as mean ± SD ($n = 3$). *** $P < 0.001$.

3.2. Preparation, characterization, and the azoreductase-responsive behavior of MPAL

It has been reported that free drugs after intravenous injection failed to induce ICD in the tumor site. To construct a tumor microenvironment azoreductase responsive liposomal carrier for Mit, we synthesized an azobenzene derivative in light of numerous reductases in tumors. As displayed in Fig. 1G, 4-dodecylaniline was reacted with the acid solution of sodium nitrite in an ice salt bath to form a diazonium salt, which was then coupled with phenol under alkaline conditions at low temperature to form compound A. Subsequently, the obtained product was halogenated with 1,3-dibromopropane to yield compound B. The chemical structures of compounds A and B were characterized by ¹H NMR

(Supporting Information Figs. S1 and S2). Finally, AZO was obtained by a Hoffman alkylation reaction, and the chemical structure of which was characterized by ¹H NMR, ¹³C NMR, and ESI-MS (Supporting Information Figs. S3–S5).

AZO was used in the construction of Mit@AZO-Lipo (MAL) (Fig. 1H). It requires dissolving AZO, CHOL, and DSPE-PEG2000 in a mixed solvent of chloroform and methanol, which was then evaporated and vacuum dried to form a uniform film. To accomplish Mit loading, ammonium sulfate was introduced in the film as a protonating agent and subjected to sonication, extrusion, and a facile incubation (Fig. 1H). MAL with various molar ratios of AZO, CHOL, and DSPE-PEG2000 was prepared for screening the optimal formulation. As shown in Supporting Information Table S2, the encapsulation efficiency and

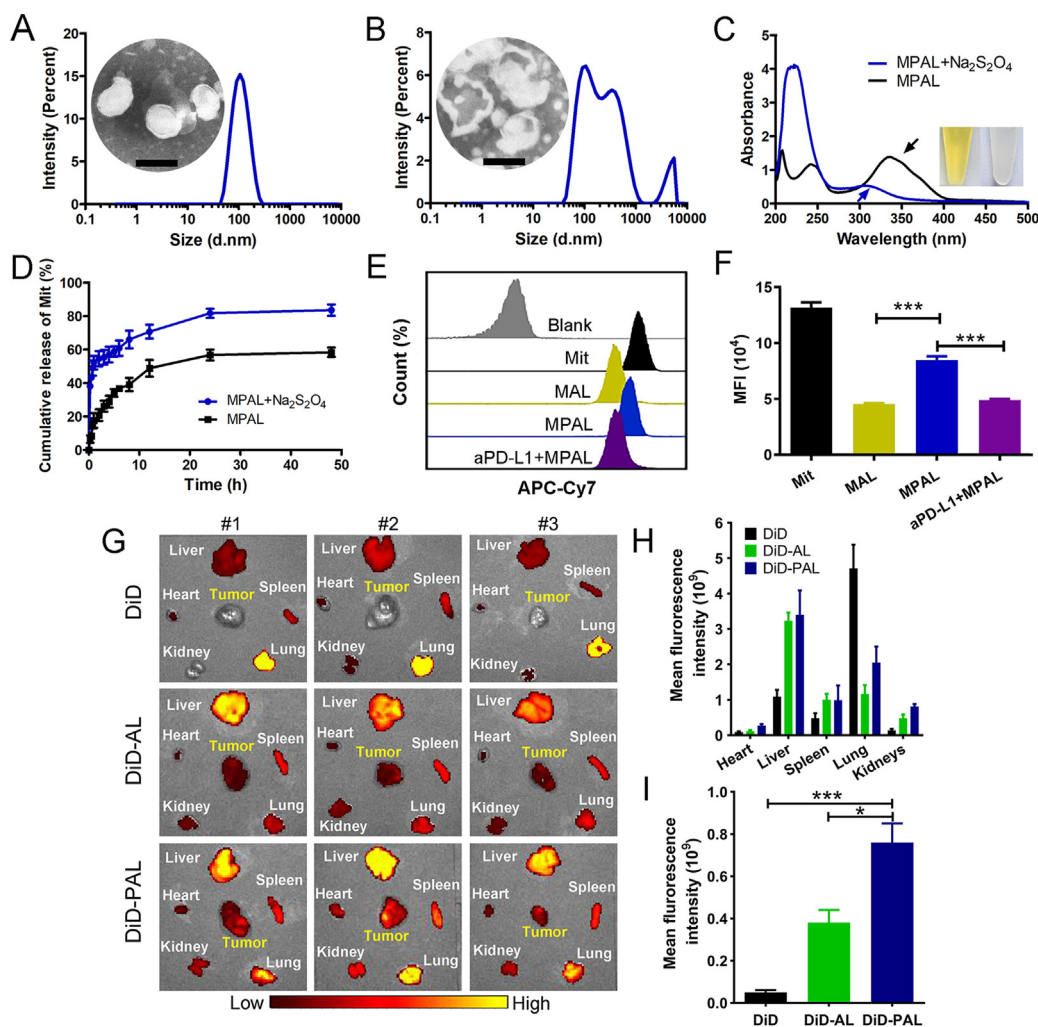


Figure 2 The azoreductase-responsive behavior and enhanced melanoma targeting capability of MPAL. (A) Size distribution and TEM image of MPAL (Scale bar: 100 nm). (B) Size distribution and TEM image of MPAL after $\text{Na}_2\text{S}_2\text{O}_4$ treatment (Scale bar: 100 nm). (C) The UV absorption spectra of MPAL and MPAL after $\text{Na}_2\text{S}_2\text{O}_4$ treatment, while the black arrow indicates the characteristic absorption peak of azo. The picture showed AL in centrifuge tubes before and after treated with $\text{Na}_2\text{S}_2\text{O}_4$. (D) The release of Mit from MPAL or MPAL after treated with $\text{Na}_2\text{S}_2\text{O}_4$ in PBS. (E) Flow cytometry histograms and (F) quantification of cellular uptake behavior. (G) *Ex vivo* fluorescence images of heart, liver, spleen, lung, kidney, and tumor after 24 h of intravenous injection of DiD, DiD-AL, and DiD-PAL in tumor-bearing mice. Quantitative fluorescence analysis of main organs (H) and tumors (I). Data are presented as mean \pm SD ($n = 3$). * $P < 0.05$, *** $P < 0.001$.

drug loading decrease with the increase in AZO molar ratio. When the molar ratio of AZO exceeds 70%, the encapsulation efficiency is lower than 20%. In addition, we also compared the particle size and polydispersity of these liposomes and obtained the optimal molar ratio of 65:30:5 for AZO, CHOL, and DSPE-PEG2000. Especially, the prepared liposomes rich in tertiary amines promoted the expression of CD83 on BMDCs (Supporting Information Fig. S6), which shows potential in controlling the maturation of CD4 and CD8 T cells and may enhance the immunogenic chemotherapy of melanoma.

To complete the insertion of aPD-L1, DSPE-PEG2000-NHS reacted with the amino group exposed on aPD-L1 to form DSPE-PEG-aPD-L1 micelles, which were then incubated with MAL and purified by ultrafiltration to obtain MPAL (Fig. 1H). To verify that aPD-L1 was successfully coupled to MAL, the liposomes were labeled with PE-labeled goat anti-rat IgG H&L antibody and results showed that the positive rate reached $82.89 \pm 2.88\%$

(Supporting Information Fig. S7). Besides, the size of MPAL was 101.2 ± 2.6 nm with a PDI of 0.10 ± 0.01 (Fig. 2A), which was an increase of about 10 nm compared to MAL. These results indicate successful chimerism of aPD-L1 in MAL.

The size of MPAL was almost unchanged in 50% fetal bovine serum (FBS) (Supporting Information Fig. S8), indicating its potential to maintain stability in blood circulation. To investigate the azoreductase response behavior of MPAL *in vitro*, $\text{Na}_2\text{S}_2\text{O}_4$ was applied to mimic the azoreductase in the tumor microenvironment (TME)³⁷. As shown in Fig. 2A and Supporting Information Fig. S9, MPAL exhibited an apparent single-layer spherical vesicle structure with uniform particle size. After $\text{Na}_2\text{S}_2\text{O}_4$ treatment, the size of MPAL was 169.8 ± 20.8 nm with a PDI of 0.41 ± 0.08 . Moreover, the morphology of MPAL became irregular and was accompanied by bilayer fracture and inclusion collapse (Fig. 2B). On the other hand, wavelength scans of MPAL before and after the $\text{Na}_2\text{S}_2\text{O}_4$ treatment were performed by

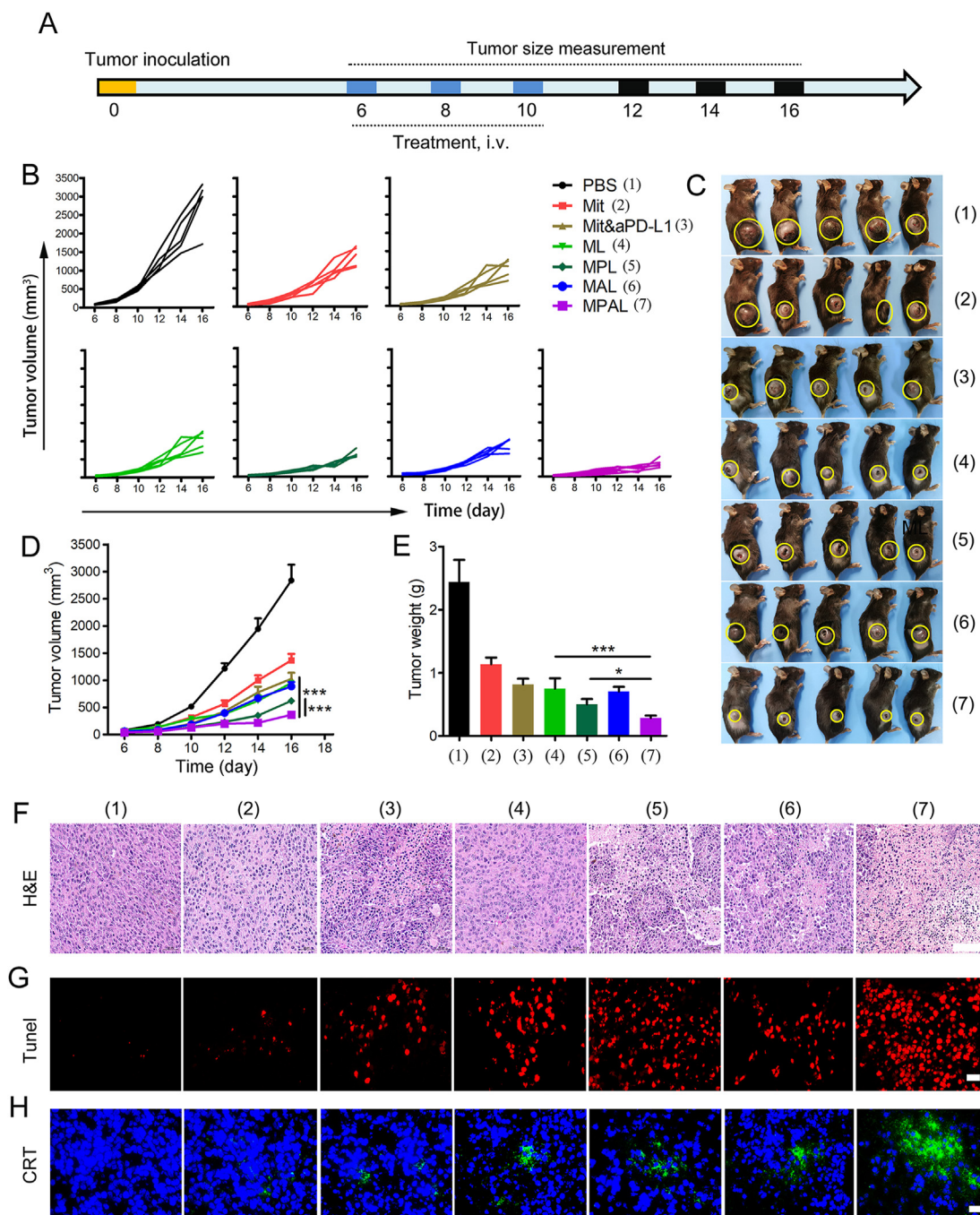


Figure 3 Therapeutic activity of MPAL in B16–F10 subcutaneous xenograft model ($n = 5$). (A) Outline of inoculation, treatment, and tumor volume measurement. (B) Individual tumor growth kinetics in various groups. (C) Photographs of mice in each group on day 17 after inoculation, and yellow circles represent tumor sites. (D) Mean tumor volume growth curves of mice in each group (Results are presented as mean \pm SEM, *** $P < 0.001$). (E) Tumor weight of mice in each group on day 17 after inoculation. (F) H&E staining of tumor sections in each group (scale bar: 50 μ m). TUNEL (G) and CRT immunofluorescence staining (H) of tumor sections in each group (Scale bar: 20 μ m).

UV–visible spectrophotometry. As demonstrated by the arrow in Fig. 2C, the characteristic broad absorption at around 340 nm of MPAL corresponding to AZO disappeared completely after $\text{Na}_2\text{S}_2\text{O}_4$ treatment. It can also be found that the color of AL had changed from bright yellow to colorless after being treated with $\text{Na}_2\text{S}_2\text{O}_4$ (Fig. 2C). Encouraged by the above results, we further evaluated the responsive release behavior of Mit from MPAL by dialysis. As shown in Fig. 2D, Mit was slowly released from

MPAL without $\text{Na}_2\text{S}_2\text{O}_4$, and the cumulative release was $58 \pm 4.9\%$ within 48 h. As a comparison, MPAL showed appreciably burst release behavior of Mit after $\text{Na}_2\text{S}_2\text{O}_4$ treatment, and the cumulative release was $83.7 \pm 3.4\%$ within 48 h. The reason for the faster release rate of Mit from $\text{Na}_2\text{S}_2\text{O}_4$ -treated MPAL could be explained by that $\text{Na}_2\text{S}_2\text{O}_4$ causes single-electron reduction of AZO in MPAL to form aniline derivatives accompanied by covalent bond cleavage and reduced lipid layer stability,

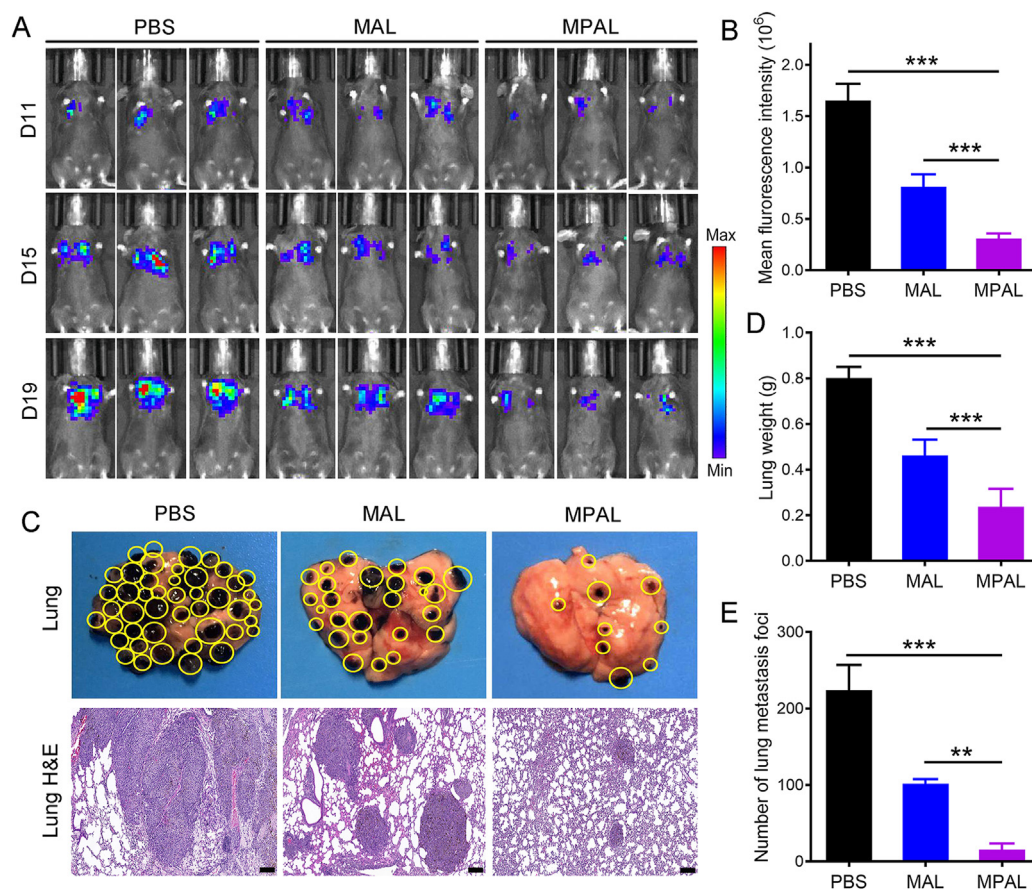


Figure 4 Therapeutic activity of MPAL in the B16–F10 tumor lung metastasis model. (A) *In vivo* bioluminescence imaging of B16–F10-Luc in control and treatment groups on days 11, 15, and 19, the figure shows 3 representative mice from each group ($n = 5$). Mean fluorescence intensity (B), representative pictures and H&E staining (scale bar: 200 μm) (C), weights (D), and metastatic nodules (E) of lungs in each group on day 19 after B16–F10-Luc tumor inoculation. Data are presented as mean \pm SD. $^{*}P < 0.01$, $^{***}P < 0.001$.

which further leads to liposome rupture and release of Mit. These results indicate that the dissociation of MPAL accelerates the release of Mit, and it is foreseeable that the responsive release behavior of MPAL in the presence of azoreductase will increase the local drug concentration of Mit in TME.

3.3. Enhanced melanoma targeting capability of MPAL

To investigate the melanoma targeting of MPAL, cellular uptake of MPAL in melanoma was carried out by flow cytometry. As shown in Fig. 2E and F, Mit was easier to be taken up by B16–F10 than MAL and MPAL, which might be ascribed to the passive diffusion of water-soluble drugs into cells. In addition, MPAL can significantly facilitate the uptake of Mit compared with MAL ($P < 0.001$), owing to the overexpression of PD-L1 in B16–F10 cells, and the specific binding of aPD-L1 inserted on MPAL to PD-L1 enhanced cellular uptake of MPAL through receptor-mediated endocytosis. Indeed, our results revealed that the uptake efficiency of MPAL in B16–F10 cells decreased by 42.4% compared to MPAL group when aPD-L1 was added in advance ($P < 0.001$). It is reported that tertiary amines decorated nanoparticles were positively charged at low pH conditions due to the high pH sensitivity of tertiary amines, which may interact with the naturally generated anionic phospholipids in the endosomal membrane to form ion pairs with a non-bilayer structure, resulting

in the rupture of the endosomal membrane^{38,39}. Therefore, after the internalization of MPAL, the tertiary amines on the surface of MPAL may undergo the same process to facilitate MPAL escape from lysosomes. Then, azoreductases in cytoplasm cause single-electron reduction of AZO in MPAL to reduce lipid layer stability, which further leads to MPAL rupture and release of Mit.

The ability of MAPL-induced ICD of B16–F10 cells was carried out *in vitro*. As shown in Supporting Information Fig. S10A, CRT exposure on B16–F10 cells treated with MPAL was significantly more than that on untreated cells, and as the concentration of MPAL increased, the proportion of CRT-positive cells was appreciably increased. In addition, HMGB1 was detected by flow cytometry and results showed that after MPAL treatment, the proportion of HMGB1 positive cells was significantly reduced compared with untreated cells, confirming that MPAL caused the release of HMGB1 from the nucleus (Fig. S10B). For another ICD-related DAMP, ATP in the supernatant of MPAL-treated B16–F10 cells was detected by bioluminescence-based ATP assay. Compared with the group without treatment, MPAL significantly enhanced the secretion of ATP from B16–F10 cells (Fig. S10C). These results suggest that MPAL does not affect the ability of Mit to induce ICD in B16–F10 cells, and shows a promising application in inducing ICD of B16–F10 cells *in vivo*.

To further assess the tumor targeting of liposomes *in vivo*, we established a mouse melanoma xenograft model. Considering the

weak fluorescence intensity of Mit, DiD was used as a model drug to trace liposomes. After 24 h of administration of free DiD, DiD-AL, and DiD-PAL, respectively, major organs and tumors were removed for *ex vivo* fluorescence imaging. As depicted in Fig. 2G and H, DiD fluorescence was mainly distributed in the liver and lung. Noticeably, distinct fluorescence signals were detected in tumor sites in DiD-AL and DiD-PAL groups, whereas almost no signals were detected in the free DiD group. Quantitative analysis

demonstrated that compared with free DiD, the mean fluorescence intensity of tumor in mice injected with DiD-AL increased by 2.4-fold and that in mice injected with DiD-PAL increased by 4.8-fold (Fig. 2I). Besides, compared with DiD-AL, DiD-PAL significantly promoted the accumulation of DiD in tumor tissue ($P < 0.05$). These results indicate that the prepared liposome has good melanoma targeting performance, and show the application prospects in the treatment of melanoma.

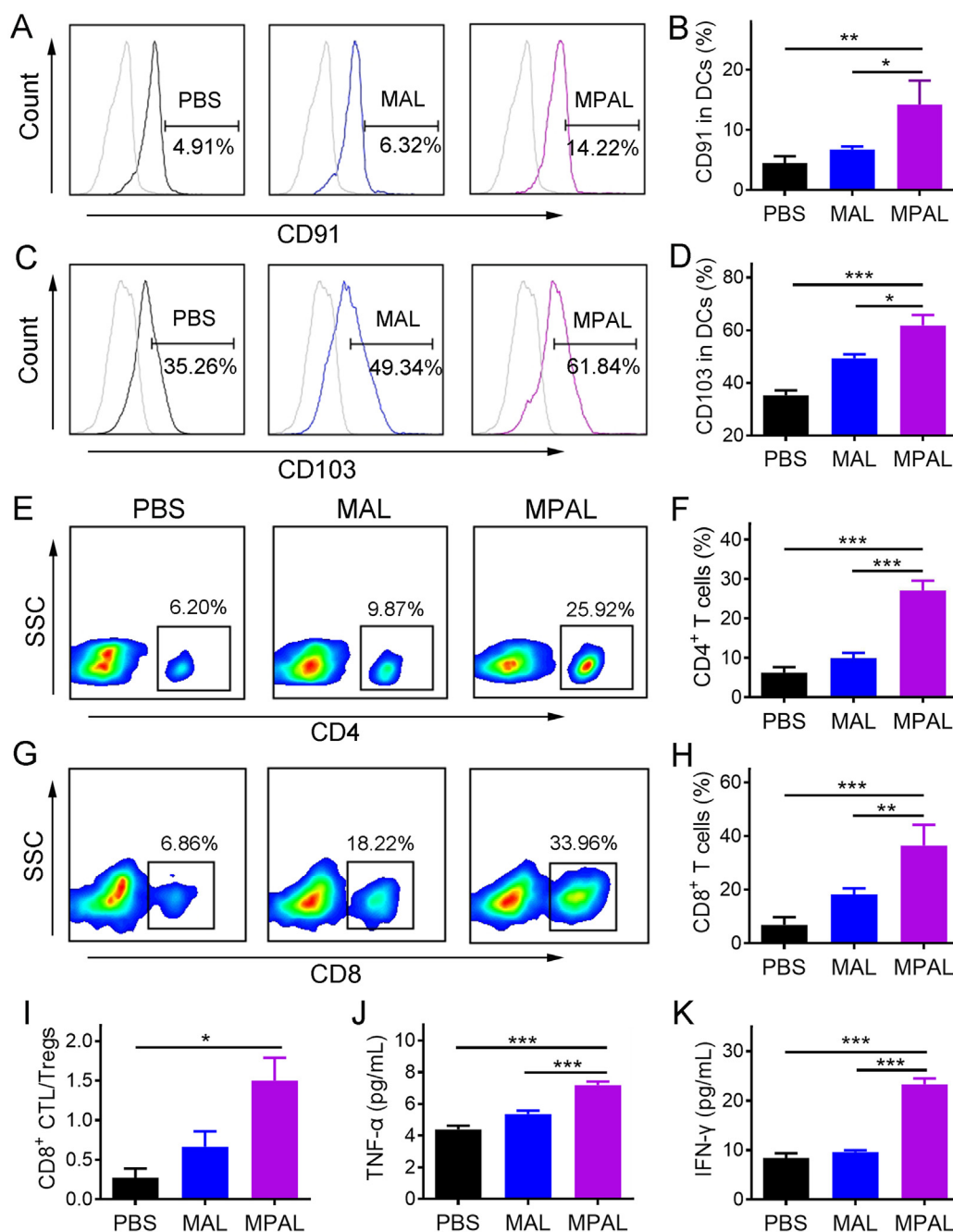


Figure 5 *In situ* tumor vaccine induced by MPAL activates and amplifies the immune response *in vivo*. (A, B) Flow cytometric analysis of CD91⁺ DCs in tumors. (C, D) Flow cytometric analysis of CD103⁺ DCs in tumor-draining lymph nodes. (E, F) Flow cytometric analysis of CD4⁺ T cells in tumors. (G, H) Flow cytometric analysis of CD8⁺ T cells in tumors. (I) The ratio of CD8⁺ T cells to Treg cells. The concentrations of TNF- α (J) and IFN- γ (K) in sera from mice after different treatments. Results are presented as mean \pm SD ($n = 3$). * $P < 0.05$, ** $P < 0.01$, *** $P < 0.001$.

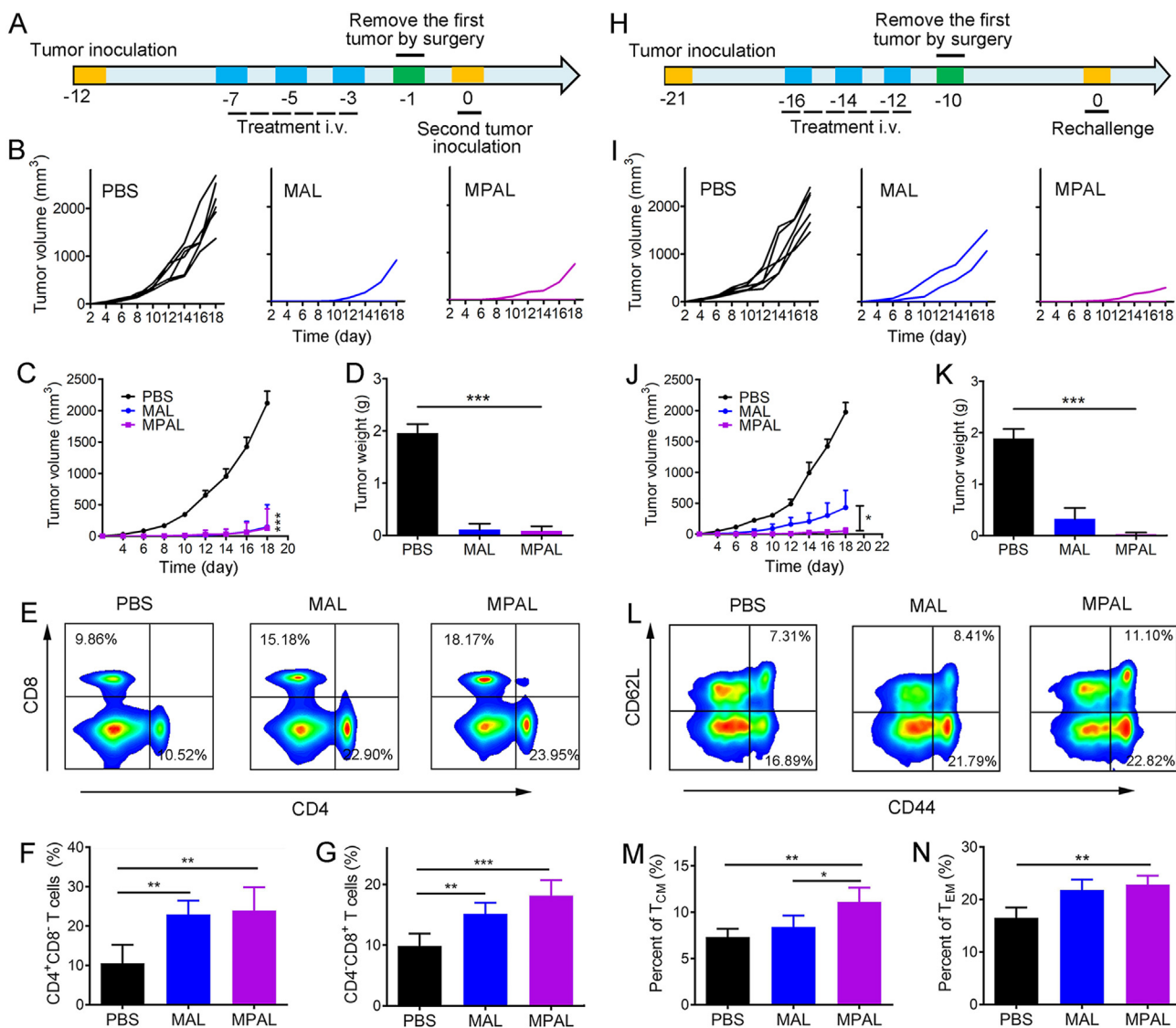


Figure 6 Neoadjuvant chemo-immunotherapy with MPAL suppressed the postsurgical metastasis and recurrence of B16–F10 tumors. (A) Schematic depicting the experimental procedure for evaluating postsurgical metastasis of B16–F10 tumors. (B) Individual tumor growth kinetics in PBS, MAL, and MPAL groups. (C) Mean tumor volume growth curves of mice in each group (Data are presented as mean \pm SEM, *** P < 0.001: MPAL versus PBS). (D) Tumor weight of mice in each group on day 19 after second tumor inoculation. (E, F, and G) Flow cytometric analysis of CD4⁺ and CD8⁺ T cells in the spleen. (H) Schematic depicting the experimental procedure for evaluation of postsurgical recurrence of B16–F10 tumors. (I) Individual tumor growth curves in PBS, MAL, and MPAL groups after tumor rechallenged. (J) Mean tumor volume growth curves of mice in each group (Data are presented as mean \pm SEM, * P < 0.05). (K) Tumor weight of mice in each group on day 19 after tumor rechallenged. (L, M, and N) Flow cytometric analysis of central memory T cells (CD44⁺CD62L^{low}, T_{CM}) and effector memory T cells (CD44⁺CD62L^{high}, T_{EM}) in the spleen (gated on CD3⁺CD8⁺ T cells, n = 5). (* P < 0.05, ** P < 0.01, *** P < 0.001).

3.4. Potent antitumor efficacy of MPAL in B16–F10 subcutaneous xenograft model

The antitumor efficiency of MPAL was evaluated in the B16–F10 subcutaneous xenograft model. As shown in Fig. 3A, on Day 6 after inoculation, mice were randomly divided into PBS, Mit, Mit&αPD-L1, ML, MPL, MAL, and MPAL groups, and they were treated once every two days for three times. Fig. 3B showed the tumor volume growth of individual mouse in each group. It can be observed that 16 days after inoculation, the tumor volume of 4 mice in the PBS group has reached 3000 mm³, which implied the malignant degree of melanoma. Surprisingly, after receiving MPAL treatment, the tumor volume in 4 mice was less than

500 mm³ on day 16 after inoculation. The inhibitory effect of various formulations on tumor growth can be observed intuitively from the photography images of mice (Fig. 3C). In addition, the tumor volume growth curve also showed that tumor growth was inhibited to varying degrees after treatment with various formulations (Fig. 3D). Notably, the tumor inhibition rates of MPL and MPAL were both over 70% which was higher than the Mit&αPD-L1 group, which reflected the enhanced therapeutic effect of Mit after encapsulation in liposomes. In addition, it was observed that the tumor volume in the MPL group was 622 \pm 91 mm³. In comparison, the MPAL group exhibited a more significant tumor inhibition effect (366 \pm 117 mm³, P < 0.001), which may be attributed to the azoreductase responsive release behavior of drugs

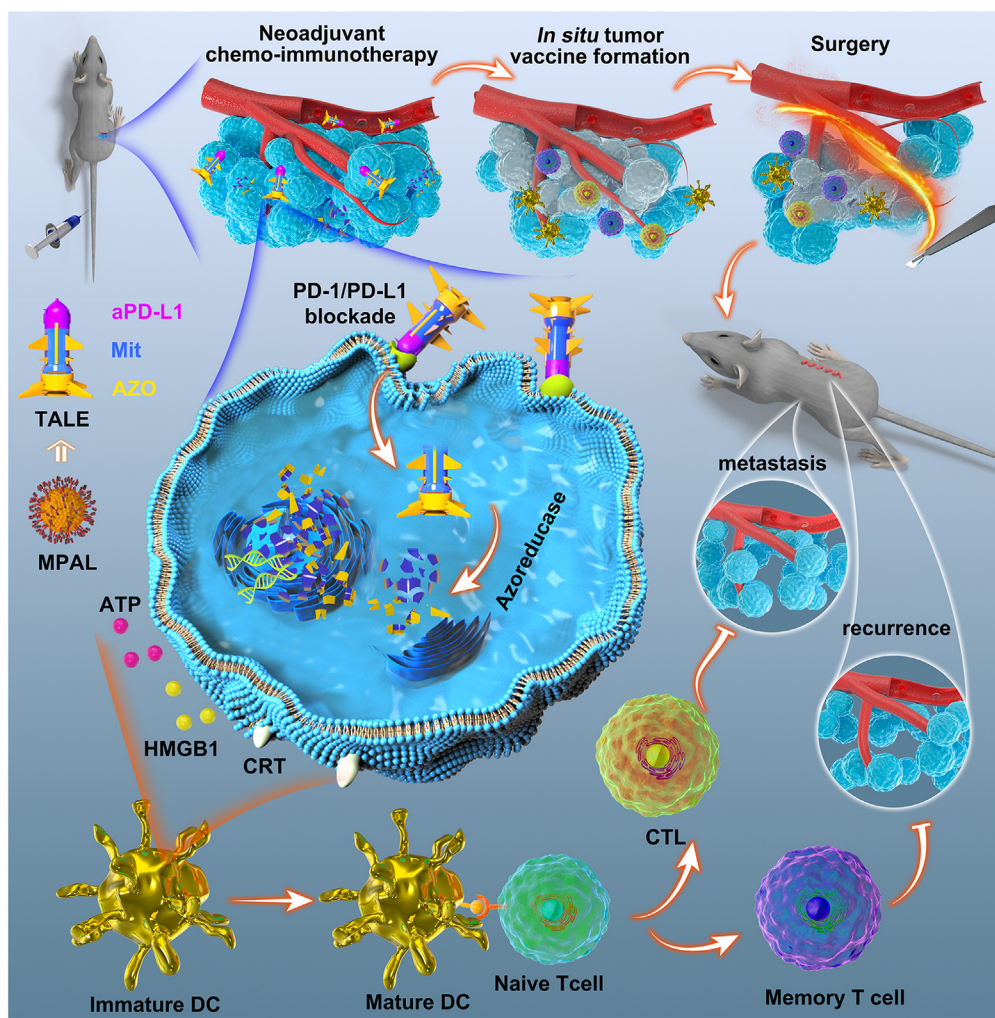


Figure 7 TALE mobilizing antitumor immunity through eliciting ICD of tumor cells and PD-1/PD-L1 blockade enables neoadjuvant chemo-immunotherapy to minimize postsurgical tumor metastasis and relapse.

in MPAL, resulting in a higher concentration of Mit in the tumor. Besides, the tumor growth in MPAL group was significantly inhibited than that in the MAL group ($366 \pm 117 \text{ mm}^3$ vs $888 \pm 181 \text{ mm}^3$) ($P < 0.001$), which may be ascribed to a better tumor targeting conferred by aPD-L1 and the concomitant blocking of PD-1/PD-L1 pathway. Similar results can also be found in the analysis of tumor weights (Fig. 3E). Our results demonstrated the potential of MPAL as an effective neoadjuvant agent for inhibition of primary tumors preoperatively.

Next, H&E staining and immunofluorescence of tumor sections were conducted to evaluate cell damage induced by various formulations. As shown in Fig. 3F, the tumors in the PBS group thrived because the cells were densely arranged and the morphology of nucleus was normal. In comparison, the number of cells in MPAL group became sparse, and the nuclei shrank into small dots, indicating that MPAL caused the highest proliferation inhibition than other treatment groups. A similar result was also found in the TUNEL assay that the MPAL group showed the highest tumor cell apoptosis (Fig. 3G). In addition, inspired by the aforementioned robust effect of Mit-mediated ICD *in vitro* and *in vivo*, CRT exposure on tumor cells induced by MPAL was evaluated. The results in Fig. 3H displayed that MPAL exhibited a more pronounced effect of inducing CRT exposure than other

formulations. Given that CRT is a crucial sign of ICD, it plays a vital role in promoting the maturation of dendritic cells and subsequent cellular immune response⁴⁰, we speculated that MPAL might bolster antitumor immunity by amplified ICD of tumor cells *in vivo*, resulting in enhanced antitumor efficacy. For the safety evaluations, blood chemistry analysis was conducted to assess liver, kidney, and cardiac toxicity in mice after treatment. The results in Supporting Information Fig. S11 showed all indexes of MPAL groups were within the normal range. In addition, a histopathologic examination was performed to assess microscopic changes in major organs (heart, liver, spleen, lung, and kidney) in mice after treatment. As shown in Supporting Information Fig. S12, no obvious pathologic occurrences were seen in the MPAL group, implying its utility as a safe neoadjuvant agent.

3.5. Effective inhibition of pulmonary metastasis by MPAL

In view of the effective tumor inhibition and *in vivo* safety of MPAL, we therefore further considered to verify the therapeutic effect of which in the B16–F10–Luc lung metastasis model. As displayed in Fig. 4A, bioluminescence imaging was performed on Days 11, 15, and 19 after tumor inoculation, respectively. It was observed that a large amount of fluorescence appeared on

Day 19 in the PBS group. As a comparison, the fluorescence intensity in the MAL group was relatively low, indicating its effective tumor inhibition ability. Interestingly, MPAL treatment could maintain the pulmonary fluorescence of mice at a weak level. The insertion of aPD-L1 contributes to a significant further improvement in antitumor metastasis, as demonstrated by mean fluorescence intensity analysis (Fig. 4B). This might be explained by the enhanced tumor targeted efficiency of MPAL and enhanced T cell immune function. Furthermore, the pulmonary tissues were collected for further evaluation of anti-metastasis efficacy. Consistent with the above results, MPAL exhibited the most substantial inhibition of B16-F10-Luc lung metastasis as indicated by lung weights, H&E staining, and the tumor nodules (Fig. 4C–E). These results confirm that MPAL could effectively inhibit the pulmonary metastasis of melanoma and had great potential in preoperative elimination of circulating tumor cells or micrometastasis that might lead to postoperative metastasis.

3.6. Antitumor immune activation by MPAL *in vivo*

After MPAL treatment, sustained tumor growth inhibition in both local tumors and pulmonary metastases prompted us to wonder whether tumor-associated antigens were generated *in situ* and performed “vaccine-like” functions with the assistance of released DAMPs and exogenous adjuvant. To elucidate our hypothesis, two days after the last treatment, the tumors and TDLNs were harvested to assess the induced innate and adaptive immune response. As shown in Fig. 5A and B, there were up to $14.22 \pm 3.97\%$ CD11c⁺CD91⁺ DCs in TME after MPAL treatment, much higher than that in PBS ($4.5 \pm 1.1\%$) and MAL group ($6.7 \pm 0.5\%$). Echoing the previous results of increased CRT exposure on tumor cells, its counter receptor (CD91) showed a similar increasing trend, which further substantiates the advantage of our strategy in inducing ICD onsite. Meanwhile, the percentage of CD103⁺ DCs in TDLN significantly increased after the treatment of MPAL ($61.8 \pm 7.9\%$) in comparison to that of MAL ($49.3 \pm 3.0\%$, $P < 0.05$) and PBS ($35.3 \pm 3.7\%$, $P < 0.001$) (Fig. 5C and D). As an important integrin receptor for DC activation, CD103 plays a critical role in promoting the activation of CD8⁺ T cells⁴¹. However, DC functions including antigen recognition and cross-presentation are normally inhibited in TME⁴². Our results suggested that MPAL-induced ICD had great potential to activate DC function, thus amplifying the CD8⁺ T mediated antitumor immunity.

Indeed, results in Fig. 5E–H confirm our hypothesis that the proportion of infiltrating helper CD4⁺ and cytotoxic CD8⁺ T cells in the tumor was significantly increased after MPAL treatment. In addition, the infiltrating Treg that can inhibit the function of CD8⁺ T cells was pronounced decreased in the MPAL group ($10.2 \pm 1.2\%$) compared to the PBS group ($30.8 \pm 6.9\%$, $P < 0.01$) (Supporting Information Fig. S13). Moreover, the enhanced immunostimulatory environment mediated by MPAL was evidenced by the significantly increased CD8⁺ CTL/Treg ratio compared to the PBS group (Fig. 5I). As a result, the above positive regulation would lead to the secretion of various cytokines including TNF- α and IFN- γ , which play a crucial role in T-helper cell 1 type (Th1) polarization. We thus determined the concentration of TNF- α and IFN- γ in the sera of treated tumor-bearing mice, and the results showed the highest concentration of which in the MPAL group as expected (Fig. 5J and K). Collectively, these results confirm our hypothesis that an *in situ*

vaccine was formed in the tumor after intravenous injection of MPAL, and the resulting robust adaptive immune response augmented the tumor growth inhibition.

3.7. Prevention of postsurgical tumor metastasis and recurrence by MPAL as a neoadjuvant chemo-immunotherapy setting

For patients with high-risk resectable cancers, several courses of chemotherapy are usually required to reduce the circulating tumor cells and then undergo surgical resection. Nevertheless, residual microtumors around the primary tumor, or tumor cells that have entered the blood circulation, are likely to cause tumor recurrence or metastasis, and ultimately lead to the death of patients. Vaccine-like function generated *in situ* after intravenous injection of MPAL might bolster systemic immune response and contribute to the inhibition of postsurgery tumor metastasis and recurrence. We thus established the tumor model of B16-F10, and then treated mice with PBS, MAL, and MPAL, respectively. The tumors were removed two days after the last treatment by surgery, and live B16-F10 cells were inoculated on the contralateral side the next day to simulate the postsurgical metastasis (Fig. 6A). Surprisingly, MAL and MPAL both showed appreciable inhibition of tumor metastasis (Fig. 6B–D). Moreover, of the 6 mice, only one mouse tumor was monitored in MAL or MPAL-treated mice. Considering the previously confirmed increased CD8⁺ CTL accumulation in tumors, the *in situ* tumor vaccines generated after treatment may amplify the systemic immune response, thereby eradicating postsurgical metastatic tumor cells. To further validate our hypothesis, on Day -1 (Fig. 6A), the splenocyte was isolated to detect T cells. For the MAL and MPAL-treated mice, the percentage of CD3⁺ T cells in the spleen was both significantly increased compared with the PBS group (Supporting Information Fig. S14). Moreover, for T cell subtypes, the ratio of CD4⁺CD8⁻ helper T lymphocytes and CD4⁻CD8⁺ cytotoxic T lymphocytes in the spleen after MPAL treatment were both significantly higher than PBS group (Fig. 6F and G), indicating the successful induction of systemic cellular immune responses. Intriguingly, similar effects were observed in the MAL group. The probable explanation is that MAL induced effective antitumor immune responses comparable to MPAL by enhanced ICD.

To simulate the tumor postsurgical recurrence after treatment, tumor cells were rechallenged on the opposite side of the treated tumor-bearing mice that underwent surgical resection and maintained survival with tumor-free for a period of time (Fig. 6H). Notably, the tumor growth of mice after MAL treatment was significantly delayed than that of mice who received PBS (Fig. 6I). MPAL treatment appeared to be appreciably better than MAL in preventing tumor recurrence after surgery, suggesting that aPD-L1 induced an enhanced antitumor immunological memory response (Fig. 6I–K). In fact, 5 of the 6 mice had no tumor recurrence in the MPAL group and the tumor growth rate of the recurrent one was much lower than that of the PBS group and MAL group (Fig. 6I). To further identify the immunologic memory protection effect induced by MPAL, we isolated mouse splenic lymphocytes the day before rechallenge and analyzed CD8⁺ memory T cells by flow cytometry. As shown in Fig. 6L–N, for the mice received MPAL followed by surgery, both the percentage of effector memory T cells (CD3⁺CD8⁺CD44⁺CD62L⁻, T_{EM}) and central memory T cells (CD3⁺CD8⁺CD44⁺CD62L⁺, T_{CM}) in the spleen were significantly higher than that of mice received PBS plus surgery (Fig. 6M and N). However, the frequency of T_{CM} in the

MAL group was much lower than that of the MPAL group since aPD-L1 was omitted. Taken together, our data demonstrated that the vaccine-like function generated *in situ* after intravenous injection of MPAL could indeed boost the immunological memory responses in mice and effectively inhibited the postsurgical recurrence of tumors.

4. Conclusions

Neoadjuvant chemotherapy has become an important pillar in the treatment of high-risk resectable cancers, with the aim of increasing the feasibility of R0 resection and avoiding futile surgery. However, it is still fraught with risks of postoperative tumor metastasis and recurrence⁴³. Most chemotherapeutics can only delay tumor growth, while growing evidence reveals that the generation of anti-tumor immune response and potent tumor infiltration of CD8⁺ T cells are vital to durable tumor remissions^{44,45}. On the other hand, the combination of immune checkpoint inhibitors (ipilimumab and nivolumab) in the neoadjuvant immunotherapy of melanoma was found to improve clinical outcomes, but was associated with considerable toxicity¹. Unlike current neoadjuvant therapeutic strategies, the TALE system integrated immunogenic chemotherapy and checkpoint blockade therapy has been engineered and shown main advantages in inducing primary tumor cell immunogenic death and generating a strong anti-tumor immune response to inhibit postoperative metastasis and recurrence. Effective preoperative anti-tumor immunity triggered by TALE depends on adequate drug actions on melanoma and host adaptive immune activation.

Mit-induced ICD of B16–F10 cells had been substantiated in our *in vitro* and *in vivo* results (Fig. 1). Nonetheless, considering the low accumulation of chemotherapeutics in tumor sites, it is essential to increase the Mit load at tumor sites in order to cause the ICD of tumor cells. In our work, Mit was encapsulated in the TALE which was equipped with aPD-L1. Upon systemic administration *in vivo*, TALE reached the tumor microenvironment by activating targeting and underwent swift disintegration to burst release of Mit mediated by intracellular azoreductases (Fig. 7). It is noteworthy that TALE increased drug accumulation in tumors by 4.8-fold compared with free drugs (Fig. 2I). To our knowledge, this is the first study of neoadjuvant chemo-immunotherapy using nanotechnology to combine immunogenic chemotherapeutic agents with checkpoint inhibitors. We also found the potent antitumor efficacy of TALE in the B16–F10 subcutaneous xenograft model and pulmonary metastasis model without severe side effects (Figs. 3 and 4, and Figs. S11 and S12).

Extensive preoperative immune activation requires a variety of different T cell cloning activation, which depends on broad antigen release³⁰. The resulting ICD after TALE treatment appeared to generate an *in situ* tumor vaccine depot containing DAMPs and all tumor antigens in the primary tumor, which could be more likely to bolster antitumor immunity compared with the reported tumor vaccines composed of one or several antigens. In addition, our tactic avoided the cumbersome preparation process of tumor vaccines, which may address the technical bottlenecks, treatment cost, and time cost faced by tumor antigen preparation, especially neoantigens. Moreover, the dying B16–F10 cells enhanced the recruitment and activation of dendritic cells in tandem with tertiary amine compounds, and further amplified CD8⁺ T cell

response owing to the PD-1/PD-L1 pathway blockade, resulting in elevated CD8⁺ CTL/Treg ratio in tumor tissues, and increased CD8⁺ T cells and effector memory T cells frequencies in the spleens. Thus, neoadjuvant chemo-immunotherapy with TALE altered tumor immunosuppressive microenvironment while generating long-term systemic immunosurveillance that can be transformed into durable tumor remissions. Therefore, TALE may pave a new way for neoadjuvant chemo-immunotherapy to advance the prevention of postsurgical tumor metastasis and recurrence.

Acknowledgments

This work was financially supported by the National Natural Science Foundation of China (82172094), Funds of Sichuan Province for Distinguished Young Scholar (2021JDJQ0037, China), and 1.3.5 project for disciplines of excellence, West China Hospital, Sichuan University (ZYYC08002, China). We also appreciate Hui Wang from the Analytical & Testing Center of Sichuan University for her help with SEM characterization.

Author contributions

Changyang Gong, Tao He and Qinjie Wu designed the research. Tao He carried out the experiments, performed data analysis and wrote the manuscript. Mingxing Hu, Shun Yao Zhu, Meiling Shen, and Xiaorong Kou assisted experiments. Xiuqi Liang, Lu Li, Xinchao Li, and Miaomiao Zhang participated part of the experiments. All of the authors have read and approved the final manuscript.

Conflicts of interest

The authors report no conflicts of interest.

Appendix A. Supporting information

Supporting data to this article can be found online at <https://doi.org/10.1016/j.apsb.2022.09.017>.

References

1. Amaria RN, Reddy SM, Tawbi HA, Davies MA, Ross MI, Glitza IC, et al. Neoadjuvant immune checkpoint blockade in high-risk resectable melanoma. *Nat Med* 2018;**24**:1649–54.
2. Ho WJ, Zhu QF, Durham J, Popovic A, Xavier S, Leatherman J, et al. Neoadjuvant cabozantinib and nivolumab convert locally advanced hepatocellular carcinoma into resectable disease with enhanced anti-tumor immunity. *Nat Cancer* 2021;**2**:891–903.
3. Gao JJ, Navai N, Alhalabi O, Siefker-Radtke A, Campbell MT, Tidwell RS, et al. Neoadjuvant PD-L1 plus CTLA-4 blockade in patients with cisplatin-ineligible operable high-risk urothelial carcinoma. *Nat Med* 2020;**26**:1845–51.
4. Montemurro F, Nuzzolese I, Ponzzone R. Neoadjuvant or adjuvant chemotherapy in early breast cancer?. *Expert Opin Pharmacother* 2020;**21**:1071–82.
5. Pataer A, Weissferdt A, Vaporciyan AA, Correa AM, Sepesi B, Wistuba II, et al. Evaluation of pathologic response in lymph nodes of patients with lung cancer receiving neoadjuvant chemotherapy. *J Thorac Oncol* 2021;**16**:1289–97.

6. Glynne-Jones R, Anyamene N, Moran B, Harrison M. Neoadjuvant chemotherapy in MRI-staged high-risk rectal cancer in addition to or as an alternative to preoperative chemoradiation?. *Ann Oncol* 2012;**23**: 2517–26.
7. Liu HJ, Wang JF, Wang MM, Wang YZ, Shi SS, Hu XX, et al. Biomimetic nanomedicine coupled with neoadjuvant chemotherapy to suppress breast cancer metastasis via tumor microenvironment remodeling. *Adv Funct Mater* 2021;**31**:2100262.
8. Symmans WF, Wei CM, Gould R, Yu X, Zhang Y, Liu M, et al. Long-term prognostic risk after neoadjuvant chemotherapy associated with residual cancer burden and breast cancer subtype. *J Clin Oncol* 2017; **35**:1049–60.
9. Haldar R, Ben-Eliyahu S. Reducing the risk of post-surgical cancer recurrence: a perioperative anti-inflammatory anti-stress approach. *Future Oncol* 2018;**14**:1017–21.
10. Bu LL, Yan JJ, Wang ZJ, Ruan HT, Chen Q, Gunadhi V, et al. Advances in drug delivery for post-surgical cancer treatment. *Bio-materials* 2019;**219**:119182.
11. Zhang W, Wang F, Hu C, Zhou Y, Gao HL, Hu J. The progress and perspective of nanoparticle-enabled tumor metastasis treatment. *Acta Pharm Sin B* 2020;**10**:2037–53.
12. Melero I, Gaudernack G, Gerritsen W, Huber C, Parmiani G, Scholl S, et al. Therapeutic vaccines for cancer: an overview of clinical trials. *Nat Rev Clin Oncol* 2014;**11**:509–24.
13. Luo ZC, He T, Liu P, Yi ZG, Zhu SY, Liang XQ, et al. Self-adjuvanted molecular activator (SeaMac) nanovaccines promote cancer immunotherapy. *Adv Healthcare Mater* 2021;**10**:2002080.
14. Ye XY, Liang X, Chen Q, Miao QW, Chen XL, Zhang XD, et al. Surgical tumor-derived personalized photothermal vaccine formulation for cancer immunotherapy. *ACS Nano* 2019;**13**:2956–68.
15. Li L, Zou JH, Dai YL, Fan WP, Niu G, Yang Z, et al. Burst release of encapsulated annexin A5 in tumours boosts cytotoxic T-cell responses by blocking the phagocytosis of apoptotic cells. *Nat Biomed Eng* 2020; **4**:1102–16.
16. Kroemer G, Galluzzi L, Kepp O, Zitvogel L. Immunogenic cell death in cancer therapy. *Annu Rev Immunol* 2013;**31**:51–72.
17. Fan YC, Kuai R, Xu Y, Ochyl LJ, Irvine DJ, Moon JJ. Immunogenic cell death amplified by co-localized adjuvant delivery for cancer immunotherapy. *Nano Lett* 2017;**17**:7387–93.
18. Huang H, Jiang CT, Shen S, Liu A, Gan YJ, Tong QS, et al. Nano-enabled reversal of IDO1-mediated immunosuppression synergizes with immunogenic chemotherapy for improved cancer therapy. *Nano Lett* 2019;**19**:5356–65.
19. Lin YX, Wang Y, Ding JX, Jiang AP, Wang J, Yu M, et al. Reactivation of the tumor suppressor PTEN by mRNA nanoparticles enhances antitumor immunity in preclinical models. *Sci Transl Med* 2021;**13**: eaba9772.
20. Ren H, Yong JH, Yang QQ, Yang Z, Liu ZY, Xu Y, et al. Self-assembled FeS-based cascade bioreactor with enhanced tumor penetration and synergistic treatments to trigger robust cancer immunotherapy. *Acta Pharm Sin B* 2021;**11**:3244–61.
21. Ladoire S, Mignot G, Dabakuyo S, Arnould L, Apetoh L, Rébé C, et al. *In situ* immune response after neoadjuvant chemotherapy for breast cancer predicts survival. *J Pathol* 2011;**224**:389–400.
22. Abbott DE, Merkow RP, Cantor SB, Fleming JB, Varadhachary GR, Crane C, et al. Cost-effectiveness of treatment strategies for pancreatic head adenocarcinoma and potential opportunities for improvement. *Ann Surg Oncol* 2012;**19**:3659–67.
23. Pol J, Vacchelli E, Aranda F, Castoldi F, Eggermont A, Cremer I, et al. Trial watch: immunogenic cell death inducers for anticancer chemotherapy. *OncoImmunology* 2015;**4**:e1008866.
24. Li Q, Zhou YX, He WD, Ren XM, Zhang MZ, Jiang Y, et al. Platelet-armed nanoplatform to harmonize janus-faced IFN- γ against tumor recurrence and metastasis. *J Control Release* 2021;**338**:33–45.
25. Li QQ, Shi ZQ, Zhang F, Zeng WW, Zhu DW, Mei L. Symphony of nanomaterials and immunotherapy based on the cancer–immunity cycle. *Acta Pharm Sin B* 2022;**12**:107–34.
26. Zhang F, Lu GH, Wen XL, Li F, Ji XY, Li QQ, et al. Magnetic nanoparticles coated with polyphenols for spatio-temporally controlled cancer photothermal/immunotherapy. *J Control Release* 2020;**326**: 131–9.
27. Sang W, Zhang Z, Dai YL, Chen XY. Recent advances in nanomaterial-based synergistic combination cancer immunotherapy. *Chem Soc Rev* 2019;**48**:3771–810.
28. Jia RX, Teng LS, Gao LY, Su T, Fu L, Qiu ZD, et al. Advances in multiple stimuli-responsive drug-delivery systems for cancer therapy. *Int J Nanomed* 2021;**16**:1525–51.
29. Peng JR, Xiao Y, Yang Q, Liu QY, Chen Y, Shi K, et al. Intracellular aggregation of peptide-reprogrammed small molecule nanoassemblies enhances cancer chemotherapy and combinatorial immunotherapy. *Acta Pharm Sin B* 2021;**11**:1069–82.
30. Yang WJ, Zhu GZ, Wang S, Yu GC, Yang Z, Lin L, et al. *In situ* dendritic cell vaccine for effective cancer immunotherapy. *ACS Nano* 2019;**13**:3083–94.
31. He T, Liang XQ, Li L, Gong SL, Li XC, Zhang MM, et al. A spontaneously formed and self-adjuvanted hydrogel vaccine triggers strong immune responses. *Mater Des* 2021;**197**:109232.
32. Li H, Fan C, Lu HM, Feng CL, He PL, Yang XQ, et al. Protective role of berberine on ulcerative colitis through modulating enteric glial cells–intestinal epithelial cells–immune cells interactions. *Acta Pharm Sin B* 2020;**10**:447–61.
33. Arabi L, Badiee A, Mosaffa F, Jaafari MR. Targeting CD44 expressing cancer cells with anti-CD44 monoclonal antibody improves cellular uptake and antitumor efficacy of liposomal doxorubicin. *J Control Release* 2015;**220**:275–86.
34. Ma DD, Huang CX, Zheng J, Zhou WY, Tang JR, Chen WJ, et al. Azoreductase-responsive nanoprobe for hypoxia-induced mitophagy imaging. *Anal Chem* 2019;**91**:1360–7.
35. Luo SH, Liu YC, Wang FY, Fei Q, Shi B, An JC, et al. A fluorescent turn-on probe for visualizing lysosomes in hypoxic tumor cells. *Analyst* 2016;**141**:2879–82.
36. Galluzzi L, Buqué A, Kepp O, Zitvogel L, Kroemer G. Immunogenic cell death in cancer and infectious disease. *Nat Rev Immunol* 2017;**17**: 97–111.
37. Hu MX, Yang C, Luo Y, Chen F, Yang FF, Yang SP, et al. A hypoxia-specific and mitochondria-targeted anticancer theranostic agent with high selectivity for cancer cells. *J Mater Chem B* 2018;**6**: 2413–6.
38. Liu HM, Xie YD, Zhang YF, Cai YF, Li BY, Mao HL, et al. Development of a hypoxia-triggered and hypoxic radiosensitized liposome as a doxorubicin carrier to promote synergetic chemo-/radio-therapy for glioma. *Biomaterials* 2017;**121**:130–43.
39. Semple SC, Akinc A, Chen JX, Sandhu AP, Mui BL, Cho CK, et al. Rational design of cationic lipids for siRNA delivery. *Nat Biotechnol* 2010;**28**:172–6.
40. Gardai SJ, McPhillips KA, Frasch SC, Janssen WJ, Starefeldt A, Murphy-Ullrich JE, et al. Cell-surface calreticulin initiates clearance of viable or apoptotic cells through trans-activation of LRP on the phagocyte. *Cell* 2005;**123**:321–34.
41. Broz ML, Binnewies M, Boldajipour B, Nelson AE, Pollack JL, Erle DJ, et al. Dissecting the tumor myeloid compartment reveals rare activating antigen-presenting cells critical for T cell immunity. *Cancer Cell* 2014;**26**:638–52.
42. Veglia F, Gabrilovich DI. Dendritic cells in cancer: the role revisited. *Curr Opin Immunol* 2017;**45**:43–51.
43. Versluis JM, Long GV, Blank CU. Learning from clinical trials of neoadjuvant checkpoint blockade. *Nat Med* 2020;**26**:475–84.
44. Pfirschke C, Engblom C, Rickelt S, Cortez-Retamozo V, Garris C, Pucci F, et al. Immunogenic chemotherapy sensitizes tumors to checkpoint blockade therapy. *Immunity* 2016;**44**:343–54.
45. Zhai WJ, Zhou XM, Wang HF, Li WQ, Chen GY, Sui XH, et al. A novel cyclic peptide targeting LAG-3 for cancer immunotherapy by activating antigen-specific CD8⁺ T cell responses. *Acta Pharm Sin B* 2020;**10**:1047–60.